2007

Enhancing the detection and classification of coral reef and associated benthic habitats: A hyperspectral remote sensing approach

Deepak R. Mishra
University of Nebraska - Lincoln

Sunil Narumalani
University of Nebraska - Lincoln, snarumalani1@unl.edu

Donald Rundquist
University of Nebraska - Lincoln, drundquist1@unl.edu

Merlin P. Lawson
University of Nebraska-Lincoln, mlawson1@unl.edu

R. Perk
University of Nebraska-Lincoln, rperk1@unl.edu

Enhancing the detection and classification of coral reef and associated benthic habitats: A hyperspectral remote sensing approach

Deepak R. Mishra,[1] Sunil Narumalani,[1] Donald Rundquist,[1] Merlin Lawson,[2] and R. Perk[2]

Received 21 August 2006; revised 9 February 2007; accepted 24 April 2007; published 24 August 2007.

[1] Coral reefs and associated benthic habitats are heterogeneous in nature. A remote sensor designed to discriminate these environments requires a high number of narrow, properly placed bands which are not currently available in existing satellite sensors. Optical hyperspectral sensors mounted on aerial platforms seem to be appropriate for overcoming the lack of both high spectral and spatial resolution of satellite sensors. This research presents results of an innovative coral reef application by such a sensor. Using hyperspectral Airborne Imaging Spectroradiometer for Applications (AISA) Eagle data, the approach presented solves the confounding influence of water column attenuation on substrate reflectance on a per-pixel basis. The hyperspectral imagery was used in band ratio algorithms to derive water depth and water column optical properties (e.g., absorption and backscattering coefficients). The water column correction technique produced a bottom albedo image which revealed that the dark regions comprised of sea grasses and benthic algae had albedo values ≈15%, whereas sand- and coral-dominated areas had albedos >30% and ≈15–35%, respectively. The retrieved bottom albedo image was then used to classify the benthos, generating a detailed map of benthic habitats, followed by accuracy assessment.

Citation: Mishra, D. R., S. Narumalani, D. Rundquist, M. Lawson, and R. Perk (2007), Enhancing the detection and classification of coral reef and associated benthic habitats: A hyperspectral remote sensing approach, *J. Geophys. Res.*, *112*, C08014, doi:10.1029/2006JC003892.

1. Introduction

[2] Remote sensing techniques have been employed by many researchers to map general benthic habitat types (e.g., sand, sea grass, corals, and hard substrate) in reef environments. While multispectral, aircraft- and satellite-based observations have been available for some time [e.g., *Lyzenga*, 1978, 1981; *Biña et al.*, 1979; *Jupp et al.*, 1985; *Jupp*, 1986; *Kuchler et al.*, 1988; *Bierworth et al.*, 1993; *Mumby et al.*, 1998a], only recently have reef-scale, long-duration studies been performed [*Dustan and Halas*, 1987]. Hyperspectral data in particular offer a high potential for characterizing and mapping coral reefs because of their capability to identify individual reef components on the basis of their detailed spectral response [*Clark et al.*, 1997; *Holasek et al.*, 1998; *Holden and LeDrew*, 1999; *Hochberg and Atkinson*, 2000]. *Holden and LeDrew* [1999] have shown that a high-resolution in situ spectral library can be developed to differentiate between various coral types as well as bleached coral substrate. Hyperspectral remote sensing has also shown significant promise in distinguishing coral species and reef health. For example, *Myers et al.* [1999] describe how optical spectra can be used to differentiate between pigmented and bleached coral and coral versus macroalgae. However, research on coral reef habitats using airborne hyperspectral imagery is somewhat limited.

[3] The monitoring of coral reefs by means of remote sensing is complicated by variations arising from changes in water depth, bottom type, and water attenuation (scattering and absorption in the water column by chlorophyll, suspended sediments, colored dissolved organic matter, etc.). Substrate reflectance and water column properties (depth, absorption, and scattering coefficient) are intimately associated. Thus conventional analytical methods are unable to resolve a single parameter accurately unless the other is already known [*Lyzenga*, 1981; *Maritorena et al.*, 1994; *Mobley et al.*, 1993; *Mumby et al.*, 1998b; *Holden and LeDrew*, 1998, 2001, 2002]. Several of these works demonstrate that the wavelength specific nature of attenuation caused by the water should be removed using correction algorithms. Such algorithms would treat the coral reef as a lambertian lower boundary at a specified depth and perform corrections for the ocean/atmosphere interface, marine aerosol conditions, and light attenuation by seawater. Several models exist (e.g., Hydrolight), or are under development to perform such corrections, however they are generally designed for analysis and modeling of a single spectrum

[1]Center for Advanced Land Management Information Technologies, School of Natural Resources, University of Nebraska, Lincoln, Nebraska, USA.
[2]Department of Geosciences, University of Nebraska, Lincoln, Nebraska, USA.

0148-0227/07/2006JC003892

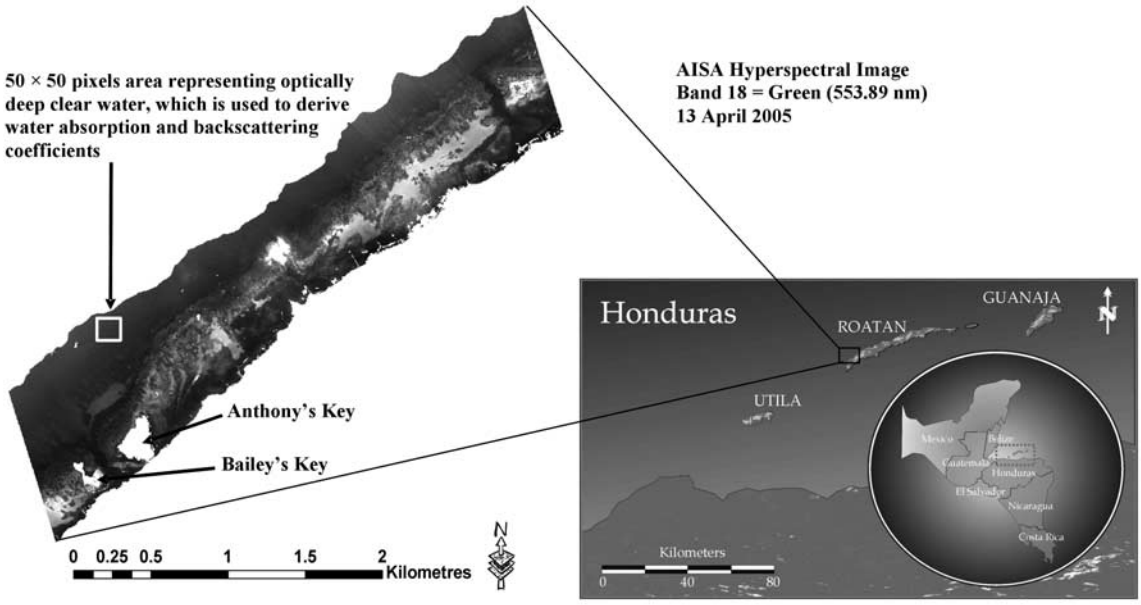

Figure 1. Location of Roatan Island, Honduras, in Central America (circle inset) and a gray scale image map of the Airborne Imaging Spectroradiometer for Applications (AISA) Eagle (band 18; 553.89 nm) acquired in April 2005.

and not for full-image, per-pixel correction of hyperspectral data. Limited examples are available of the application of water column corrections to field or modeled spectra [*Young et al.*, 1995; *Clark et al.*, 2000; *Holden and LeDrew*, 2000, 2001, 2002; *Kutser et al.*, 2003; *Mobley et al.*, 2003] or directly to hyperspectral data [*Gao et al.*, 2000; *Goodman et al.*, 2003].

[4] The approach presented in this research solves the confounding influence of water column attenuation on substrate reflectance to allow characterization of benthic habitats from hyperspectral imagery on a per-pixel basis. Airborne Imaging Spectroradiometer for Applications (AISA) Eagle hyperspectral imagery was used to derive water depth and water optical properties. These parameters were subsequently used in various bio-optical algorithms to deduce bottom albedo and ultimately to produce a benthic habitat map.

2. Study Area

[5] Roatan Island lies between 16°15′ to16°25′N and 86°22′ to 86°37′W. It is the largest of the Bay Islands of Honduras and is located in the western portion of the Caribbean Sea approximately 50 km north of the mainland. Our study was conducted in the vicinity of Anthony's Key and Man of War Key resorts on the north shore of the island (Figure 1). The reefs of the Bay Islands contain at least 52 species of stony corals, at depths ranging from 2 to 15 m [*Keck*, 2000]. Coral species include Star corals (*Montastrea annularis, M. franksi, M. faveolata,* and *M. cavernosa*), Brain corals (*Colpophylia natans, Diploria spp.*), Sheet and Lettuce corals (*Agaricia agaricites, A. larcki, A. undata, A. fragilis, and Leptosiris cuculatta*), Flower coral (*Eusmillia fastigiata*), Pillar coral (*Dendrogyra cylindrus*), Boulder Brain coral (*Colpophylia natans*), Symmetrical Brain coral (*Diploria strigosa*) and Massive Starlet coral (*Siderastrea siderea*). The bays contain highly productive sea grass beds, with Turtle Grass (*Thalassia testudinum*) being the most abundant species at Roatan. The sea grasses provide habitat for anemones, mollusks, crabs, shrimp, and many other organisms.

3. Materials and Methods

3.1. In Situ Data

[6] Data collection took place during 10–15 April 2005 along the northwestern coast of Roatan Island. Two independent in situ data sets were collected for model calibration and validation respectively. The model (bathymetry) calibration data sets were obtained from 1 m below the air/water interface by a vertically stable buoy guided along a series of transects. This buoy served as a platform for a Trimble TDC1 Asset Surveyor GPS antenna, a Sony Hi-8 mm TRV-320 digital video camera encased in a T-9 housing (Undersea Video Housings), and a Lowrance depth transducer (Figure 2). The data that were acquired by the buoy included geographic location, depth, and a photograph of the bottom. However, recorded images and the GPS synchronous time stamp were of suitable quality to determine the primary benthic cover at sample locations. A towed sensor platform (the ''towfish'') built by Shark Marine (St. Catharines, Ontario, Canada) was used to acquire the model (bathymetry, atmospheric correction, and benthic classification) validation data sets (Figures 3a and 3b). The towfish was constructed to resist wave action, so it moved through the water at a relatively constant, horizontal position while being towed at a speed of approximately 3 km/h (Figure 3c). Depths were logged continu-

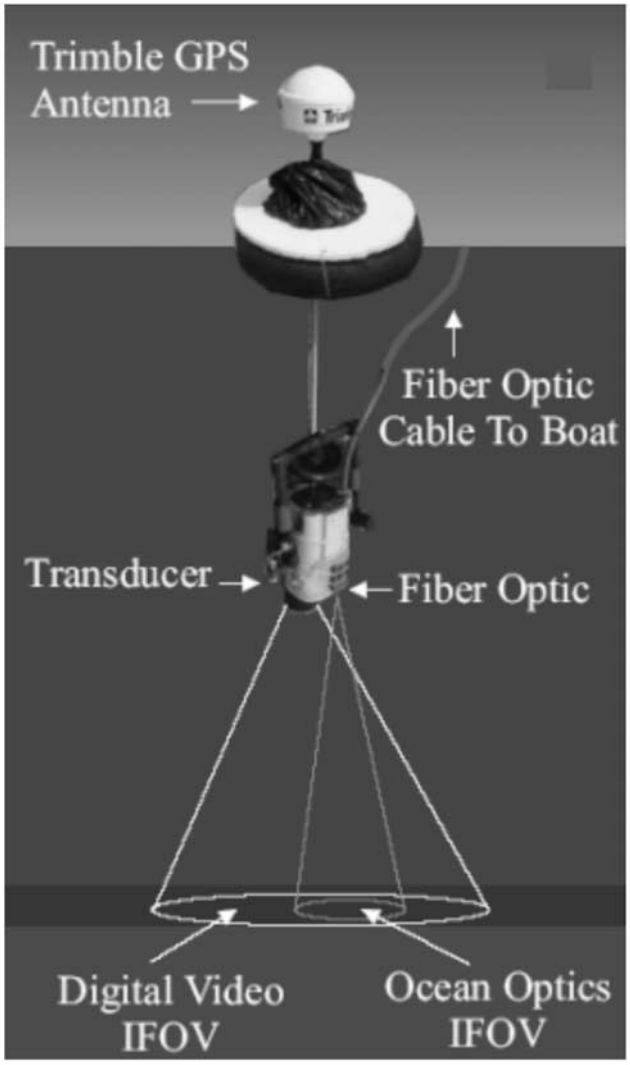

Figure 2. Components of a vertically stable GPS buoy used in in situ data collection for bathymetry model calibration. IFOV is instantaneous field of view.

ously along selected transects and a high-resolution "mini-camera" imaged the bottom at the locations where these readings were acquired (Figure 3d). A differential GPS was placed on the towfish to acquire the coordinates (Figure 3c). Two pairs of Ocean Optics USB 2000 hyperspectral radiometers were attached to the towfish (i.e., upward looking and downward looking Ocean Optics sensor) for acquiring upwelling radiance (L_u) and downwelling irradiance (E_d) just above and below the water surface. In essence the towfish provided us with four different kinds of data sets at a particular geographic location, including bottom type (photograph from the camera), depth (transducer), above-water remote sensing reflectance, $R_{rs}(\lambda)$ (Ocean Optics), and underwater remote sensing reflectance, $r_{rs}(\lambda)$ (Ocean Optics).

3.2. Airborne Hyperspectral Data

[7] An aerial remote sensing platform for hyperspectral data collection was used for this investigation. The instrument array included an AISA Eagle hyperspectral imager from Visible to Near Infrared (VNIR), a system which can provide high spatial and spectral resolution. The AISA Eagle is a solid-state, push-broom instrument that has the capability of collecting data within a spectral range of 390–1000 nm in up to 512 bands. The full spectral mode is useful for acquiring spectral signatures of specific targets in a continuum so that the data can be used to generate pure end-members and/or be used for band selection purposes. However, the large quantities of data generated would make it difficult to perform a reasonable analysis on the data; therefore images are often acquired in 10–70 spectral bands depending on the aircraft speed, altitude and mission goals. The sensor has an Inertial Navigation System (INS) and Differential Global Positioning System (DGPS) in order to provide spatially accurate data. Pitch, roll, and yaw are encoded with the DGPS information to provide accurate locations of areas of interest on the ground. The placement of the spectral bands may be configured by the user and the selected bandwidths can range anywhere from ~2 nm to ~10 nm. The AISA Eagle preprocessing software provides for the automatic geometric correction, rectification, mosaicking, and calculation of at-platform radiance by applying calibration coefficients referenced to well-characterized spectroradiometric targets (IKONOS relative spectral response and radiometric cal coefficients, Space Imaging Corporation, 2004, available at http://www.spaceimaging.com/products/ikonos/spectral.htm.). The algorithm uses the DGPS and attitude information from the INS to perform geometric, georeferencing and mosaicking operations [*Mäkisara et al.*, 1994].

[8] AISA Eagle data used for the study were acquired between 0330 and 0430 hours (CST) on 13 April 2005 when the solar zenith angle was close to 70°. Ground data indicated low wind (~3 m s^{-1}), minimal ocean swell, high visibility (30 km), and clear skies. The sensor altitude was (2.073 km), and the image was acquired at nadir at a spatial resolution of 2 m and spectral resolution of 62 bands ranging from 392.39 to 981.68 nm with a 12-bit radiometric output and the flight lines covered an area of approximately 1.6 km^2 in the vicinity of Anthony's Key and Man of War Key (Figure 1). The image data were converted to at-platform radiance by applying the calibration coefficients provided by AISA processing software "Caligeo" for subsequent processing.

[9] When extracting aquatic information, it is useful to eliminate all upland and terrestrial features [*Jensen et al.*, 1991]; thus all upland features, as well as boats, piers, and clouds, were masked out of the image. The "land-mask" restricts the spectral range of brightness values (BVs) to aquatic features and allows for detailed feature discrimination. Radiance values of the NIR band were used to prepare the binary mask which was subsequently applied to all bands. The image had ~2% cloud cover, which was successfully masked out, but cloud shadows on the water bodies still remained and could not be removed because their radiance values were similar to the other water areas.

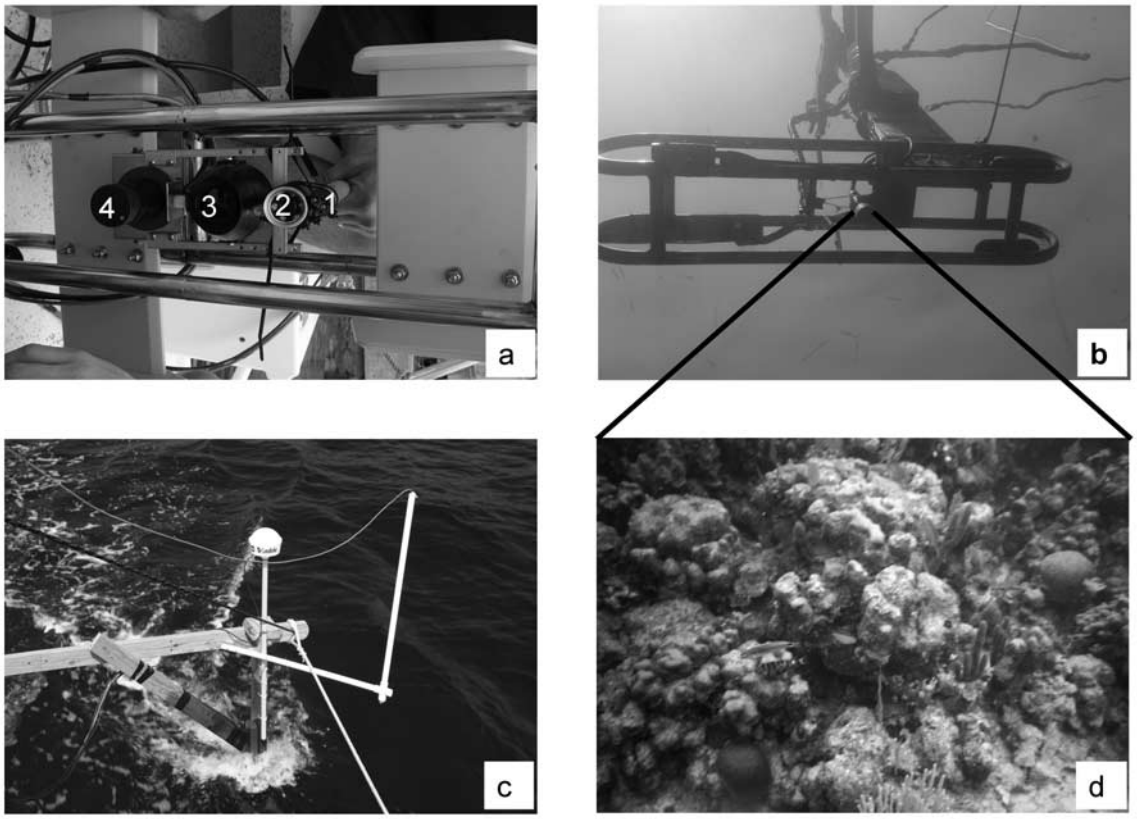

Figure 3. (a) Components of towfish, a multisensor platform designed by Center for Advanced Land Management Information Technologies (CALMIT), which includes (1) Ocean Optics hyperspectral sensor, (2) camera one, (3) camera two, and (4) transducer. (b) View of towfish from under water. (c) Towfish in action. (d) Typical coral bottom types photograph taken by towfish camera.

3.3. Atmospheric Correction

[10] The goal of atmospheric correction over the ocean is to remove the contributions of scattering in the atmosphere and reflection from the sea surface from the top of atmosphere (TOA) radiances measured by a sensor in the visible region of the spectrum. The quantity retrieved is water-leaving remote sensing reflectance, which is then used in retrieval of the water column and benthic habitat optical properties. In the case of oceanic remote sensing, the total signal received at the sensor altitude is only 8% to 10% of the signal corresponding to the oceanic water reflectance [*Gordon and Morel*, 1983]. Therefore one of the most critical steps in hyperspectral remote sensing of ocean water is to correct for atmospheric effects, in order to retrieve the top of water column radiance from the image. AISA Eagle data were atmospherically corrected by using Fast Line-of-Sight Atmospheric Analysis of Spectral Hypercubes (FLAASH), a first-principles atmospheric correction algorithm for visible to shortwave infrared (SWIR) hyperspectral data.

[11] FLAASH atmospheric correction uses MODTRAN code and typically consists of three steps [*Matthew et al.*, 2003]. The first is the retrieval of atmospheric parameters, most notably an aerosol description (the visibility or optical depth) and the column water amount. The second step in the correction is the solution of the radiative transfer equation provided below, for the given aerosol and column water vapor, and transformation to reflectance. FLAASH uses the standard equation for spectral radiance at the sensor level L in the solar wavelength range (neglecting thermal emission) from a flat Lambertian surface or its equivalent [*Vermote et al.*, 1994]:

$$L = \frac{A\,R_{rs}}{\left(1 - R^{e}_{rs}S\right)} + \frac{B\,R^{e}_{rs}}{\left(1 - R^{e}_{rs}S\right)} + L_a, \tag{1}$$

where R_{rs} is the pixel surface reflectance, R^{e}_{rs} is the surface reflectance averaged over the pixel and a surrounding region, S is the spherical albedo of the atmosphere, L_a is the radiance backscattered by the atmosphere, and A and B are the coefficients that depend on atmospheric and geometric conditions.

[12] Each of these variables depends on the spectral range of the selected channel (the wavelength index has been omitted for simplicity). The first term in equation (1) corresponds to radiance that is reflected from the surface and travels directly into the sensor. The second term corresponds to radiance from the surface that scattered by the atmosphere into the sensor, resulting in a spatial blending, or adjacency, effect.

[13] The solar zenith and azimuth angles were calculated in the algorithm from the AISA flight date, time, latitude,

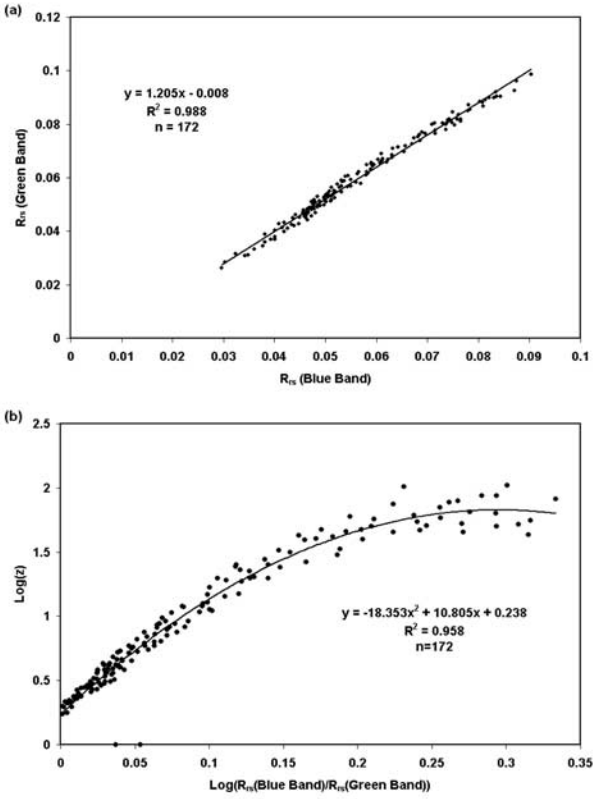

Figure 4. (a) Model calibration data set taken from GPS buoy showing the regression between blue versus green R_{rs} values for several bottom types. (b) Relationship between bottom depth and ratio of blue to green R_{rs} (equation (2)). The polynomial equation shown in the graph was used to derive bathymetry map for the study site.

and longitude and were used to predict incident solar irradiance at the top of the atmosphere. A scale factor file for the input radiance image was provided to the algorithm. The input atmospheric and aerosol models were chosen to be tropical and maritime respectively with initial visibility of 30 km. Then 820 nm band was selected as the water absorption feature, and the aerosol scale height and CO_2 mixing ratio were kept as default, which is 2.0 km and 390 ppm, respectively.

3.4. Per-Pixel Bathymetry Estimation (z)

[14] Water depth information is fundamental in discriminating and characterizing coral reef habitats, and also allows estimation of bottom albedo, which can improve benthic habitat mapping [*Mumby et al.*, 1998b]. In our research, per-pixel bathymetric knowledge was used to eliminate the change in reflectance that is attributable to variable depth, and water column attenuation effects, while deriving bottom albedo. The theoretical basis of deriving bathymetry was developed by *Lyzenga* [1978, 1981] and expanded by *Philpot* [1989]. *Maritorena et al.* [1994] demonstrated the validity of, and problem involved with, using passive remote sensing for determination of water depth.

[15] Although passive optical systems are limited in water penetration and constrained by water turbidity, the use of such instruments might be the only viable way to characterize either extensive or remote coral reef environments [*Stumpf et al.*, 2003]. A common problem among most studies is that the seafloor is covered by a patchwork of organisms and substrates that have different albedos, ranging from very dark (e.g., coral ~0.18) to very bright (e.g., sand ~0.4). The difficulty is that a dark object strongly absorbs light and will appear to be deeper than it really is. This effect is not as severe for bright objects, which absorb less strongly. Thus, for coral and sand at the same true depth, the coral virtually always appears to be deeper than the sand.

[16] Previous researchers have mapped water depth by assuming that a pair of wave bands can be identified such that the ratio of the reflectance in these two bands was the same for all the bottom types within a given scene [*Philpot*, 1989; *Gordon and Brown*, 1974]. The use of two bands allows separation of variations in depth from variations in bottom albedo. Following this assumption, we developed a site-specific algorithm to map high-resolution bathymetry using R_{rs} derived after atmospheric correction. Essentially, we identified a ratio of wave bands (blue and green) that is constant for all bottom types (Figure 4a). With these bands having different water absorptions, one band will have arithmetically lesser values than the other. As the depth increased, radiance of the band with higher absorption (green) decreased proportionally faster than the band with lower absorption (blue) and the radiance ratio of the blue to the green increased; whereas a change in bottom albedo affects both bands similarly [*Gordon and Brown*, 1974]. Accordingly, the change in ratio because of depth is much greater than that caused by change in bottom albedo, suggesting that different bottom albedos at a constant depth will still have the same ratio. This method also compensates implicitly for variable bottom types. The log transformed R_{rs} ratio of the two bands (blue, green) was plotted versus known depth (z) data (n = 172) from the buoy (Figure 4b), and a second-order polynomial written below was found to be the best fit to the calibration model for bathymetry estimation:

$$y = -18.353x^2 + 10.805x + 0.238, \tag{2}$$

where

$$y = \log(z), \tag{3}$$

$$x = \log\left[\frac{R_{rs}(blue; 481.39\ \text{nm})}{R_{rs}(green; 553.89\ \text{nm})}\right]. \tag{4}$$

[17] The above polynomial equation explained >98% of variation ($p < 0.001$) in the water depth calibration data set collected over five transects of various bottom types (coral, sand, sea grass, mixed: sand/coral/sea grass/algae etc.).

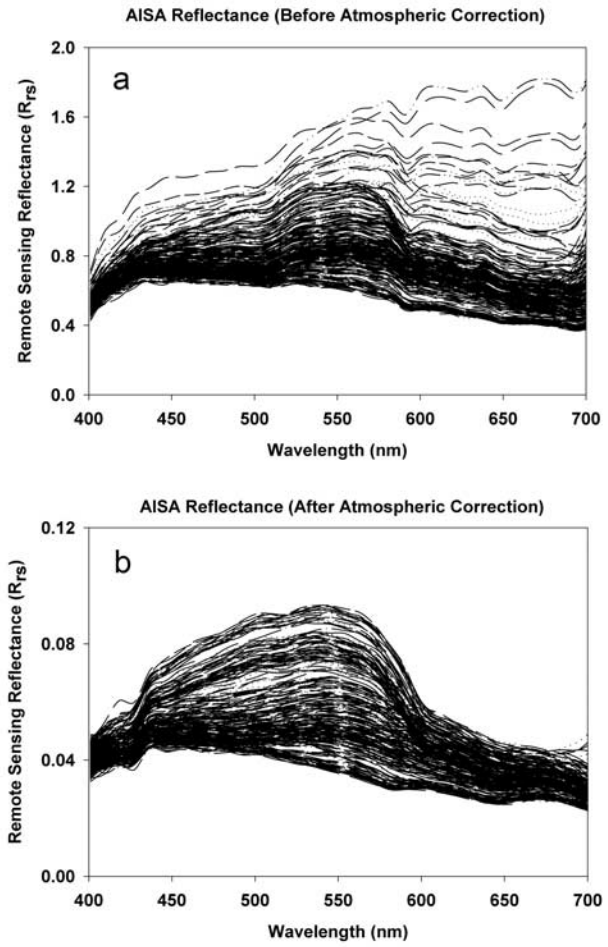

Figure 5. R_{rs} spectra of AISA Eagle pixels at all sampling locations (a) before (top of atmosphere) the image-based Fast Line-of-Sight Atmospheric Analysis of Spectral Hypercubes (FLAASH) atmospheric correction and (b) after (above water) the image-based FLAASH atmospheric correction.

Approximately 50% of the predictions were within ±0.033 m and the mean residual was ±0.17 m. Equation (2) was used to derive a map of bathymetry across the study site.

3.5. Water Column Optical Properties and Bottom Albedo Estimation

[18] The signals measured by an airborne sensor from above the water surface of a shallow marine environment are highly coupled with phytoplankton abundance (chlorophyll absorption), water column interactions (water depth, absorption by water column and scattering by suspended sediments), and bottom albedo. The apparent optical properties of water such as absorption (a) and backscattering coefficient (b_b) are the main physical agents governing the magnitude and spectral composition of the backscattered flux from the ocean surface [*Maritorena et al.*, 1994]. Derivation or approximation of these parameters are necessary in order to determine the optical bottom albedo and ultimately to map the spatial distribution of benthic habitats for shallow ocean waters. *Lee et al.* [1994, 1996] and *Zhang et al.* [1999] proposed analytical models to derive water optical properties (a and b_b) from remotely sensed data. Using AVIRIS imagery and spaceborne spectrometers with high spatial and spectral resolution, they successfully separated various shallow water constituents on the basis of their unique spectral contributions. The work described in this section of the paper demonstrates how to analytically derive bottom albedo using airborne AISA Eagle data, after the removal of atmospheric interferences.

[19] R_{rs} is defined as a ratio of the water-leaving radiance (L_w) to downwelling irradiance (E_d) just above the surface. R_{rs} is an apparent optical property [*Morel*, 1974] controlled by the absorption and scattering properties of the constituents in the water and the bottom albedo, and can be expressed as

$$R_{rs}(\lambda) = R^{w}_{rs}(\lambda) + R^{b}_{rs}(\lambda), \tag{5}$$

where $R^{w}_{rs}(\lambda)$ is the remote sensing reflectance from water column and $R^{b}_{rs}(\lambda)$ is the remote sensing reflectance from the bottom.

[20] *Lee et al.* [1994] have further approximated the two terms, $R^{w}_{rs}(\lambda)$, $R^{b}_{rs}(\lambda)$, as follows:

$$R^{w}_{rs}(\lambda) \approx 0.05\frac{b_b(\lambda)}{a(\lambda)+b_b(\lambda)}\left[1-e^{-3.2(a(\lambda)+b_b(\lambda))H}\right] \tag{6}$$

$$R^{b}_{rs}(\lambda) \approx 0.173\rho(\lambda)e^{[-2.7(a(\lambda)+b_b(\lambda))H]}, \tag{7}$$

where H is the depth of water in m (in our case it is denoted as z) and $\rho(\lambda)$ is the bottom albedo. The angular dependencies of R_{rs} (subsurface solar zenith angle, sensor zenith angle) are not explicitly stated in equations (6) and (7); however, they are included in the coefficients of the equations.

[21] The backscattering coefficient may be expressed as

$$b_b(\lambda) = b_{bp}(\lambda) + b_{bw}(\lambda), \tag{8}$$

where b_{bp} is the backscattering by particles in m^{-1} and b_{bw} is the backscattering by water molecules in m^{-1} taken from *Morel* [1974]. *Gordon et al.* [1988] and *Morel* [1988] proposed different forms of bio-optical algorithms to approximate the backscattering by particles and is incorporated in equation (8) as

$$b_b(\lambda) = b_{bp}(660)\left(\frac{660}{\lambda}\right)^{\eta} + b_{bw}(\lambda), \tag{9}$$

where η as a coefficient whose values for ocean particles range from 0.0 to 3.0 and η as 0.5 are chosen for this coastal study because it is Case-1 water, where concentration of chlorophyll and other biogenic materials is higher compared to nonbiogenic particles.

[22] To estimate b_{bp} (660), we assume there is no contribution from the bottom to the upwelling signal in AISA band 30 (656.99 nm), where the absorption is large (>0.4 m^{-1}) and dominated by water molecules. Hence, for relatively clear water deeper than $1.5/a_w(660)$, where bot-

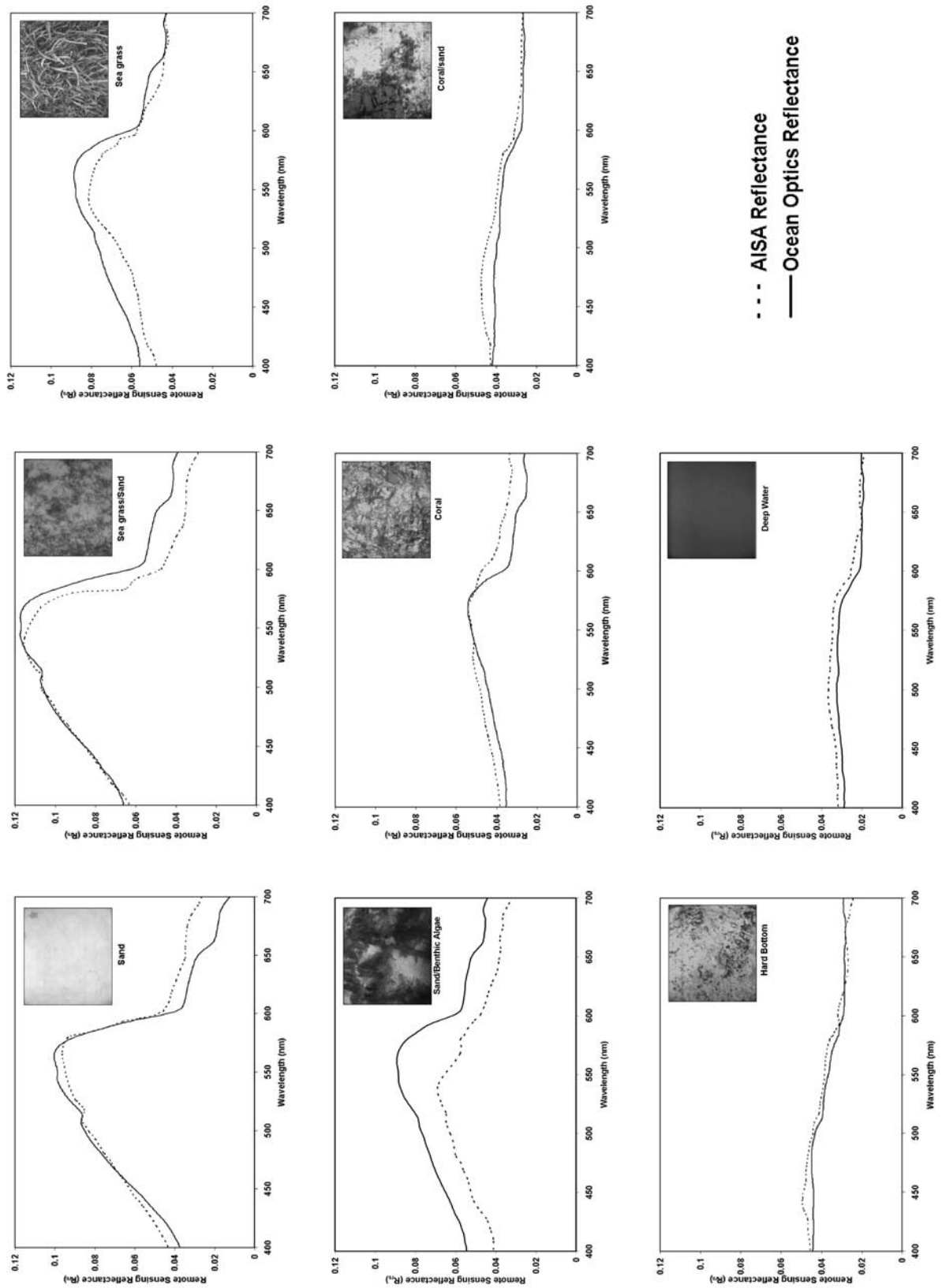

Figure 6. Comparison between the above-water R_{rs} spectra of AISA Eagle data and Ocean Optics data (in situ) for eight different bottom types. It also shows the validation of FLAASH atmospheric correction model.

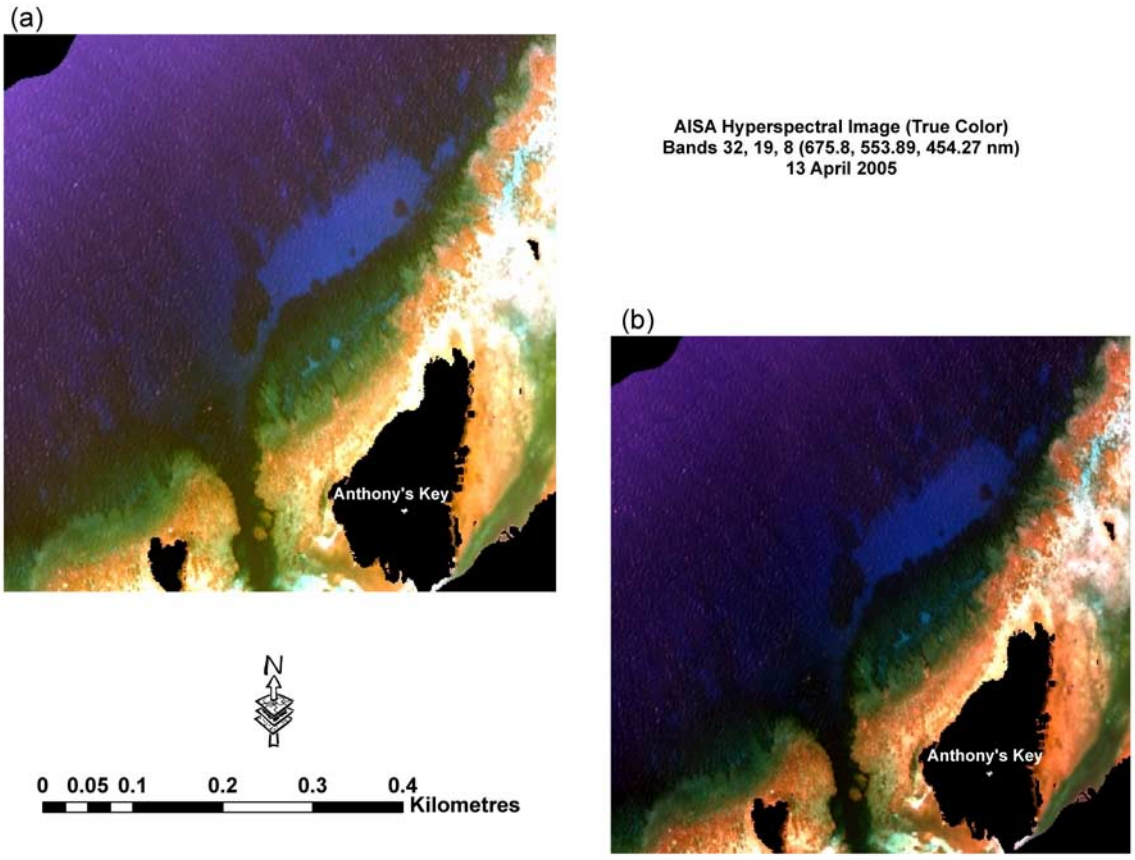

Figure 7. Visual differences in AISA true color image (RGB) (a) before the atmospheric correction and (b) after the atmospheric correction. Note that the atmospheric haziness is eliminated after the correction is applied.

tom effects are small, b_{bp} can be expressed as [*Morel and Gentili*, 1993]

$$b_{bp}(660) \approx \frac{a_w(660)}{0.05} R_{rs}(660), \tag{10}$$

where a_w is the pure-water absorption coefficient of water, taken from *Pope and Fry* [1997].

[23] The $a(\lambda)$ can be derived by modification of *Austin and Petzold* [1986] as

$$a(\lambda) = M(\lambda)[a(485) - a_w(485)] + a_w(\lambda), \tag{11}$$

where M is a statistically derived coefficient taken from *Austin and Petzold* [1986], $a(485)$ is the total absorption coefficient at 485 nm, and $a_w(485)$ is the pure-water absorption coefficient at 485 nm. According to *Lee et al.* [1998], $a(440)$, over deep water, can be empirically determined by the following equation:

$$a(440) = 10^{-0.619-1.969\left(\log_{10}\left(\frac{R_{rs}(485)}{R_{rs}(560)}\right)\right)+0.790\left(\log_{10}\left(\frac{R_{rs}(485)}{R_{rs}(560)}\right)\right)^2}, \tag{12}$$

where $R_{rs}(485)$ and $R_{rs}(560)$ are the remote sensing reflectance at 485 nm and 560 nm, respectively. We can thus rewrite equation (11) to compute the $a(485)$ as

$$a(485) = \frac{a(440) - a_w(440)}{M(440)} + a_w(485). \tag{13}$$

[24] Note that the models to derive absorption and backscattering coefficients discussed above use wavelengths such as 485, 560, and 660 nm, and in our case, applied to AISA bands 11, 20, and 30 (481.39, 563.17, 656.99 nm respectively). Equation (11) was applied over deep water pixels (white square in Figure 1) to compute the $a(\lambda)$ for the 33 bands of the AISA data set. Deep water pixels were defined as those having very little upwelling signal in the visible bands of the data set and are not affected by bottom albedo; that is, they comprise optically deep areas. A 50 $\times$ 50 pixel window was identified (white square in Figure 1) as having very little water leaving radiance values in all visible bands. The hyperspectral $a(\lambda)$ obtained from that region were assumed to be constant over the entire scene. The water optical parameters (e.g., $a(\lambda)$ and $b_b(\lambda)$) for each AISA band were derived using equations (9), (11), and (13). The water depth and optical parameters were used to derive the bottom albedo image (equation (7)) from which the

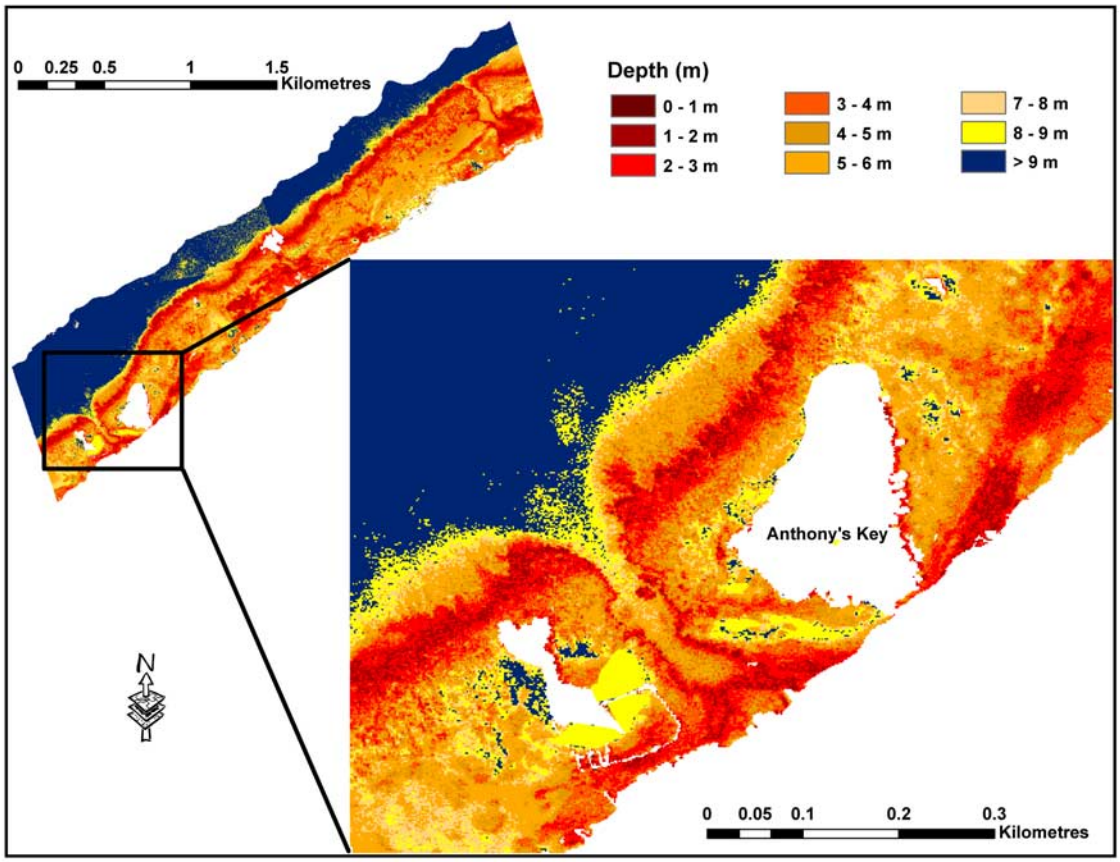

Figure 8. Bathymetric image map of Roatan Island based on the polynomial model along with a zoomed inset of Anthony's Key and Bailey's Key areas for visualizing the detail depicted by the bathymetric model.

spatial distribution of benthic habitats was extracted using standard image processing procedures.

3.6. Noise Reduction and Image Segmentation

[25] Since bottom-reflected light is negligible (specifically wavelengths >600 nm) compared to the total reflectance received at sensor level, the signal-to-noise ratio in the bottom albedo image, generated after the atmospheric and water column correction to the AISA Eagle hyperspectral image, was found to be low. Therefore a noise reduction technique or ''minimum noise fraction'' (MNF) was applied to the bottom albedo image before performing image segmentation.

[26] Prior to implementing an image segmentation algorithm, a classification scheme was developed that included the following categories: (1) sand, (2) sea grass with sand, (3) dense sea grass, (4) sand with benthic algae, (5) coral, (6) coral with sand, (7) hard bottom, (8) mixed: sand/hard bottom/coral, and (9) deep water. These nine aquatic feature classes were selected on the basis of the availability of sufficient replication of ground control data to verify feature locations in a later classification analysis. The Iterative Self Organizing Data (ISODATA) algorithm was used on the 10 MNF information bands to derive 300 clusters [*Jensen*, 2004]. Subsequently, in situ data were used to assign each cluster to a particular benthic category. Finally, a comprehensive evaluation of the classification accuracy was performed on the basis of 1208 reference points, digital still photographs, and digital video images taken by the towfish, as well as photos taken by the divers comprising our field team.

4. Results and Discussion

[27] The most common method for evaluating atmospheric correction is to compare R_{rs} spectra retrieved from the images before and after the procedure for all sampling areas as well as with ground-based measurements for a variety of targets. R_{rs} spectra from the AISA image for all sampling locations before the atmospheric correction when compared with the retrieved R_{rs} spectra after applying the image-based FLAASH model showed a significant decrease in the R_{rs} values (70–80%) (Figure 5). In the red band (600–700 nm) the R_{rs} values decreased after atmospheric correction indicating high absorption by water itself, whereas the reflectance peak in the green is caused by the scattering of suspended sediments and chlorophyll present in phytoplankton cells.

[28] To validate the accuracy of atmospheric correction, above-water R_{rs} in situ spectra acquired by the Ocean Optics hyperspectral sensor was compared with the AISA atmospherically corrected reflectance data over different benthic

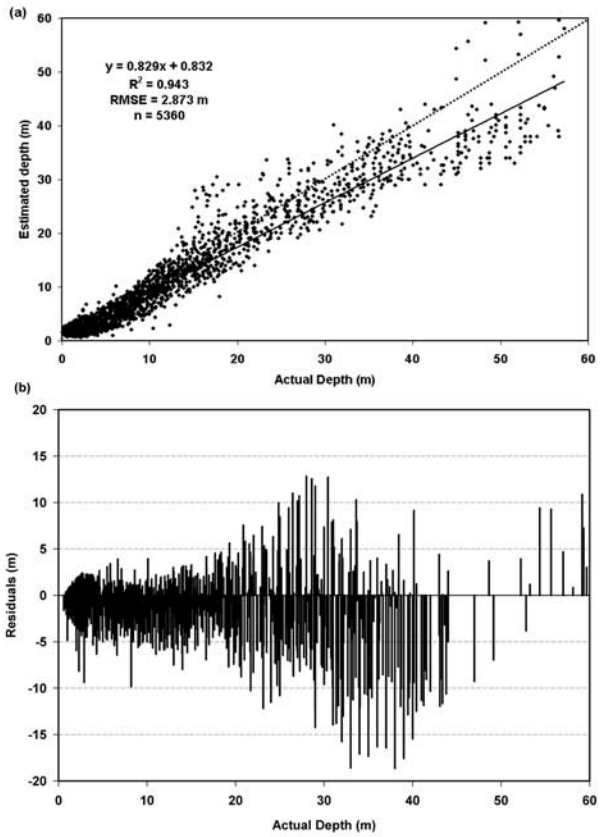

Figure 9. Depth validation: (a) plot of actual versus estimated depths using model validation data set taken from the towfish and (b) histogram plot of depth residuals from the regression model versus actual depth. Note that no particular pattern of overestimation or underestimation was observed.

habitats. Because TOA radiance values are dominated by Rayleigh and aerosol path radiance, it becomes difficult to infer the spectral properties of water over different benthic substrates. To fully understand this concept, known sample locations depicting water over eight different targets including sand, sea grass/sand, sea grass, sand/benthic algae, coral, coral/sand, hard bottom, and deep water areas were selected (Figure 6). R_{rs} spectra in shallow waters always contain a fraction of upwelling radiance of the underlying benthic habitats. When comparing R_{rs} values over shallow areas, submerged sand, or coral reefs to sand/benthic algae areas, it can be observed that the latter substrate, being darker, has a lower R_{rs}. Conversely, submerged sand (being the brightest substrate) had the maximum R_{rs} values. In general, the blue and green bands had the highest R_{rs} and the specific absorption features of different benthic bottom types were not identifiable because of the water column attenuation on the bottom reflectance spectra. Poorer agreement occurred in all bands for targets where bottom reflectance was low, such as sand/benthic algae, sea grass, and deep water areas where the absorption was strong, reflectance and signal-to-noise ratio was low. Whereas targets with high bottom reflectivity, such as sand, sea grass/sand, and coral showed increased deviation between AISA and Ocean Optics reflectance at longer wavelengths (>600 nm) because of higher light attenuation in those wavelengths. Another reason for the discrepancies between the R_{rs} values of AISA and Ocean Optics was likely caused by factors other than error in atmospheric correction, such as possible errors in the ground measurement. Yet another factor could be the not-so-perfect match of the spectral bands of AISA and the spectral configuration of the Ocean Optics spectroradiometer used for ground measurement, and thus the relative spectral responses differ between two sensors. Particularly, the spectroradiometer has a narrower bandwidth (872 bands; 400–700 nm) compared to AISA (33 bands, 400–700 nm). Overall the R_{rs} spectra of AISA and Ocean Optics sensor for all the targets were in close agreement. Visual examination of the images before and after atmospheric correction procedure showed sharp differences (Figure 7). For example, coral areas toward the northeast of Anthony's Key, which appeared to be white before the correction, showed up clearly (light brown) after the atmospheric correction. In addition, the haziness depicted in the original AISA image, attributed to Rayleigh and aerosol scattering, and water vapor content (3.3081 cm, 820 nm), was eliminated thus resulting in a visually clear image.

[29] Comparing a bathymetric map generated using equation (2) with the original AISA image (i.e., Figure 1),

Table 1. Absorption and Backscattering Coefficients Derived From the 50 × 50 Optically Deep Water Pixel Window of AISA Eagle Image[a]

Wavelength (λ), nm	a_w (λ), m^{-1}	a (λ), m^{-1}	b_{bw} (λ), m^{-1}	b_b (λ), m^{-1}	M (λ)
401.15	0.0059	0.2502	0.00285	0.00387	1.7383
409.91	0.0067	0.2425	0.00259	0.00377	1.7591
418.67	0.0078	0.2315	0.00236	0.00368	1.6974
427.42	0.0088	0.2262	0.00218	0.00359	1.6108
436.22	0.0099	0.2138	0.00199	0.00350	1.5648
445.23	0.0109	0.2002	0.00182	0.00342	1.4673
454.27	0.0118	0.1858	0.00167	0.00333	1.3627
463.31	0.0127	0.1719	0.00153	0.00326	1.2521
472.35	0.0138	0.1660	0.00141	0.00318	1.1460
481.39	0.0155	0.1544	0.00130	0.00311	1.0955
490.42	0.0181	0.1448	0.00120	0.00304	1.0000
499.46	0.0231	0.1385	0.00111	0.00297	0.9118
508.50	0.0310	0.1363	0.00103	0.00291	0.8310
517.54	0.0404	0.1410	0.00094	0.00285	0.7578
526.58	0.0425	0.1346	0.00088	0.00279	0.7241
535.61	0.0470	0.1317	0.00081	0.00274	0.6627
544.67	0.0536	0.1320	0.00076	0.00268	0.6094
553.89	0.0631	0.1366	0.00071	0.00263	0.5647
563.17	0.0693	0.1407	0.00066	0.00258	0.5289
572.45	0.0787	0.1473	0.00062	0.00253	0.5146
581.78	0.1008	0.1680	0.00057	0.00248	0.4935
591.18	0.1408	0.2089	0.00053	0.00243	0.4840
600.58	0.2295	0.3002	0.00050	0.00238	0.4903
609.98	0.2691	0.3438	0.00047	0.00234	0.5090
619.39	0.2798	0.3663	0.00044	0.00230	0.5380
628.79	0.2939	0.3911	0.00041	0.00226	0.6231
638.19	0.3076	0.4090	0.00038	0.00222	0.7001
647.59	0.3263	0.4280	0.00036	0.00218	0.7300
656.99	0.3572	0.4573	0.00034	0.00214	0.7323
666.39	0.4085	0.5015	0.00032	0.00210	0.7205
675.80	0.4223	0.5008	0.00030	0.00207	0.6693
685.20	0.4502	0.5055	0.00028	0.00204	0.5651
694.60	0.5158	0.5158	0.00027	0.00200	0.3984

[a]Pixel window is shown in Figure 1.

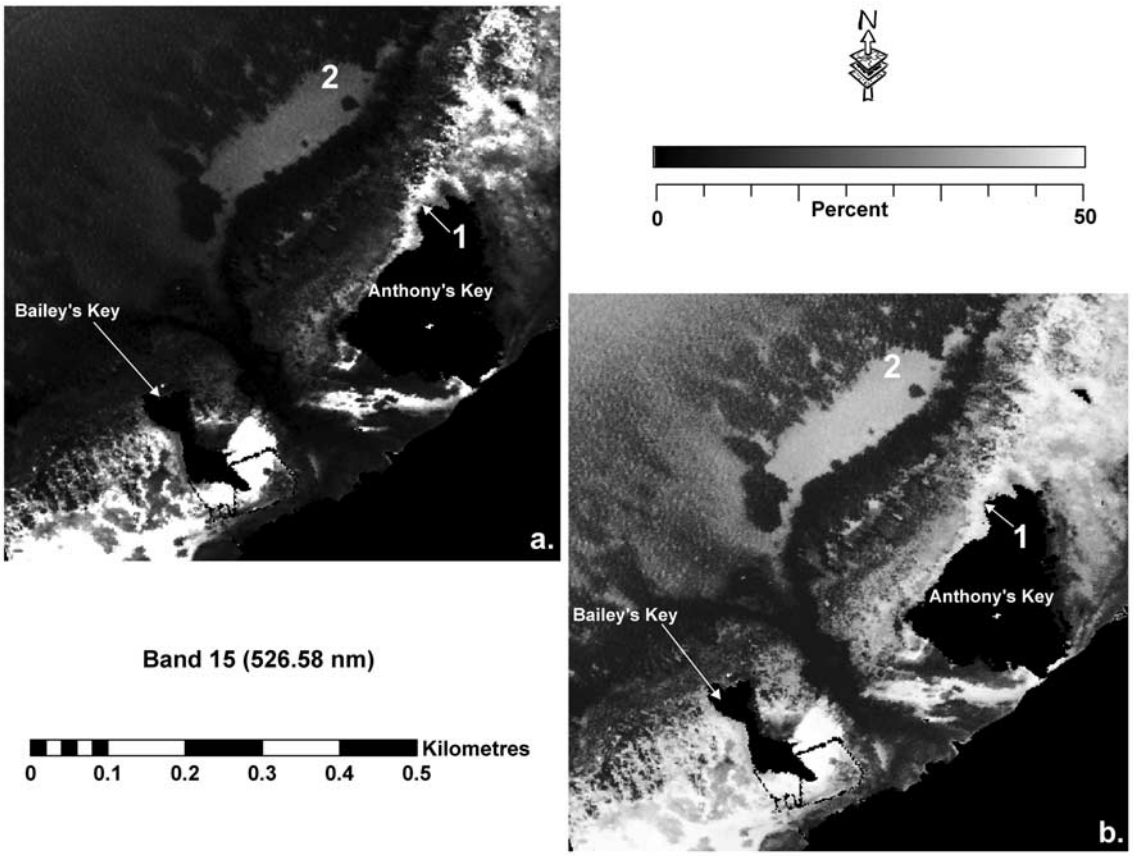

Figure 10. (a, b) Images showing bottom albedo (band 15: 526.58 nm) varying from 0 to 50% zoomed to the Key areas for visualizing the details depicted by the albedo image.

visual observations of similarities in bottom patterns can be made in both the image and the map (Figure 8). The Anthony's Key area is depicted in a large format because we have collected in situ data there annually since 2000. The spatial variation of depth in the map was high (for example, the deep channel near the Key), which is generally true in the coral reef marine environment because of their uneven morphological structure. A close examination of the image map revealed that most shallow vertical features around the Key were reproduced, including a shallow ''basin'' of sand waves, fore reef, patch reef, and step narrow reticulated reef structure. The image map also showed a clear distinction of the drop off point (depicted in blue) separating the submerged shelf-edge reef from the deep water. The barrier reef, which is separated from the shoreline by a moderately deep (usually) body of water, depicted in red color and runs SW–NE through the entire image, was the most distinct feature of the bathymetric map (Figure 8). Using 5360 in situ depth points, the bathymetric map was validated for its accuracy and the root mean square (rms) error was calculated. When analyzing the accuracies of estimated depths, it was found that the R^2 between actual depth and estimated depth was 0.943 with an RMS error of 2.873 m (Figure 9a). The slope of the trend line was found to be 0.829, which is not significantly different from the slope of 1:1 line. Residuals were calculated by subtracting estimated depths from actual depths and revealed no clear pattern of over/underestimation (Figure 9b). However, for depths >20 m the estimation error increased noticeably and the ratio transform rarely retrieved meaningful depths. This error could be due to two factors. Firstly, from the errors in model calibration, the dependence of depth with band ratio R_{rs} (blue)/R_{rs}(green) (Figure 4b) it was observed that $x \leq 0.15$, the calibration points are roughly tightly distributed around the polynomial trend line. However, for $x > 0.15$, the points are mostly deviated from the trend line thus indicating that the model incorrectly estimates depths beyond 20 m. Secondly, the ratio transform does have a greater amount of noise, which is not surprising since a ratio combination inherently amplifies small differences observed in both bands and the error variability increases with depth.

[30] The absorption and backscattering parameters for the 33 AISA bands are specified at the band centers (Table 1). Both absorption coefficients by pure water [from *Pope and Fry*, 1997] and Roatan water showed exponential increase toward the higher wavelengths (>600 nm). However, there was significant increase in absorption values observed for the blue band for Roatan water because the chlorophyll present in the phytoplankton cells absorbs blue light. Absorption by chlorophyll itself is characterized by strong absorption in the blue and red region, peaking at $\lambda \approx 430$ and 665 nm, respectively, with very little absorption in the green. Overall, as the wavelength increased, there was an increase in the total absorption coefficient, because as the wavelength increases absorption by phytoplankton pigments and water also increases. The waters off Roatan Island,

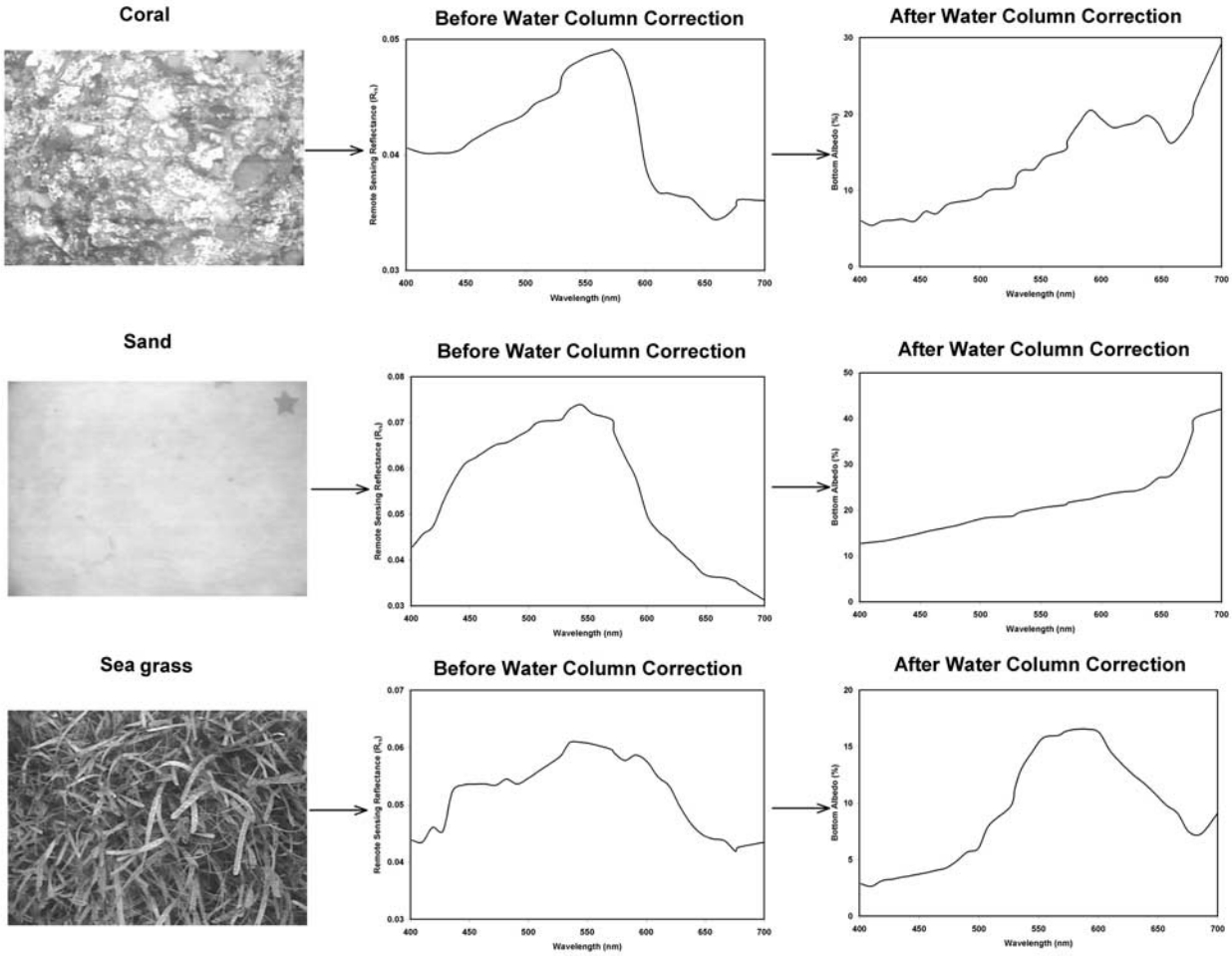

Figure 11. Comparison of above-water R_{rs} spectra (after atmospheric correction) with the bottom albedo spectra for three primary benthic features (coral, sea grass, and sand) showing the effect of water column attenuation.

where the concentration of phytoplankton (chlorophyll range: 0.031–1.81 mg/l, seston range: 0.319–4.091 mg/l, based on in situ measurements) is greater than nonbiogenic particles, are considered as Case-1 waters. Phytoplankton cells are strong absorbers of visible light and therefore play a major role in determining the absorption properties of such waters; although detritus and dissolved organic matter derived from the phytoplankton also contribute to absorption in Case-1 waters. Overall backscattering is inversely proportional to wavelength; therefore a higher coefficient was observed in blue band than in the red. Backscattering coefficients of pure water [from *Morel*, 1974] showed lower values when compared to Roatan water because of several reasons. Firstly, seawater comprises of pure water plus various dissolved salts, which average about 35 parts per thousand (35‰) by weight [*Mobley*, 1994]. These salts increase scattering above that of pure water by about 30% [*Mobley*, 1994] but have a negligible effect on absorption at visible wavelengths. Secondly, particles present in the Roatan water are generally much larger than the wavelength of visible light and are efficient scatterers, especially via diffraction, thus strongly influencing the total scattering properties of seawater.

[31] Absorption and backscattering coefficients along with water depth were incorporated in equation (7) to generate a bottom albedo image (Figure 10). Visual comparison of the atmospherically corrected image (Figure 10a) with the bottom albedo image (image generated after water column correction; Figure 10b) revealed apparent differences. For example, areas 1 and 2 (Figure 10a) are both sand bottoms, approximately 3–4 m and 9–11 m deep respectively, and showed a high contrast in their brightness values because of their occurrence at different depths. Whereas after the water column correction, that is, after eliminating the depth factor, the contrast between the two areas was similar ($\rho \approx 40\%$) (Figure 10b). The zoomed inset showed detailed variation in bottom albedo based on substrate reflectance. Dark regions are comprised of sea grasses, benthic algae with $\rho \approx 15\%$, while the bright regions represent sand-dominated areas with $\rho > 30\%$. Coral-dominated areas manifested albedos in the range of 15% to 35% depending upon the percent of live coral cover occurring in each pixel.

[32] Figure 11 shows the remarkable effect of water column attenuation while comparing above-water R_{rs} spectra (after atmospheric correction) with the bottom albedo for

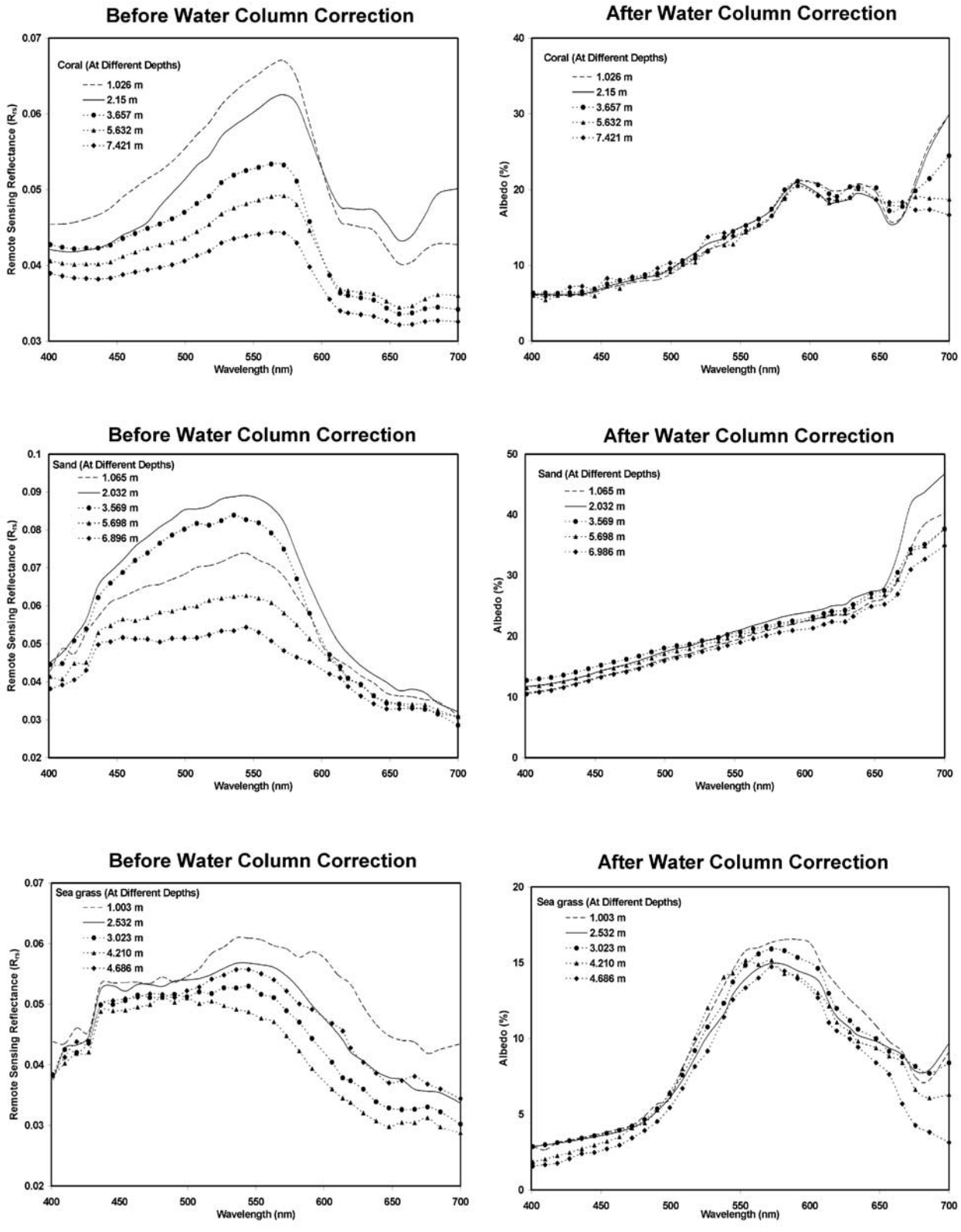

Figure 12. Validation of water column correction procedure: comparison of bottom albedo spectra of different bottom types at different depths before and after the water column correction.

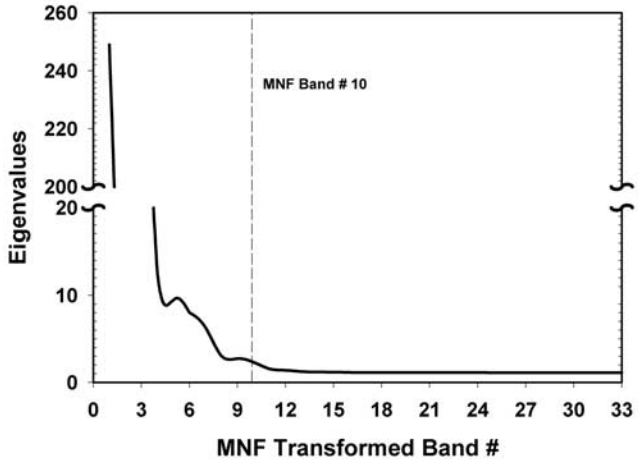

Figure 13. Eigenvalues of the minimum noise fraction (MNF)–transformed bands separating signal from noise at band 10.

three primary benthic features. Before water column correction, the three features showed similar spectral characteristics; that is, high reflectance in green and low reflectance in blue (chlorophyll absorption) and red (chlorophyll and water absorption). Any specific absorption and reflectance features for the three bottoms were not identifiable. After the water column correction, bottom albedo spectra for coral exhibited relatively low ρ between 400 to 500 nm, higher ρ between 550 and 650 nm, a narrow chlorophyll absorption feature at 675 nm, and very rapidly increasing ρ at wavelengths greater than 680 nm. This variability in the shape of coral ρ, determined by spectral absorption and fluorescence properties of multiple pigments residing at various locations in a coral colony, including the zooxanthellae and ectodermal and endodermal host tissues [*Dove et al.*, 1995], was absent in the spectra prior to the water column correction. All those spectral features became prominent after removing the water attenuation factor from the spectra. For sand bottom, a gradual increase in ρ was observed with increasing wavelength, which is a typical sand reflectance characteristic. Sea grass bottom type exhibited a reflectance peak at around 550 nm, and chlorophyll absorption features at $\sim$675 nm and both chlorophyll and caretinoid absorption in blue band. Overall, the water absorption and suspended sediment scattering played an important role and photons reflected back from benthos were basically mixed spectra with significant contributions from water column, specifically in the red wavelengths. After water column removal,

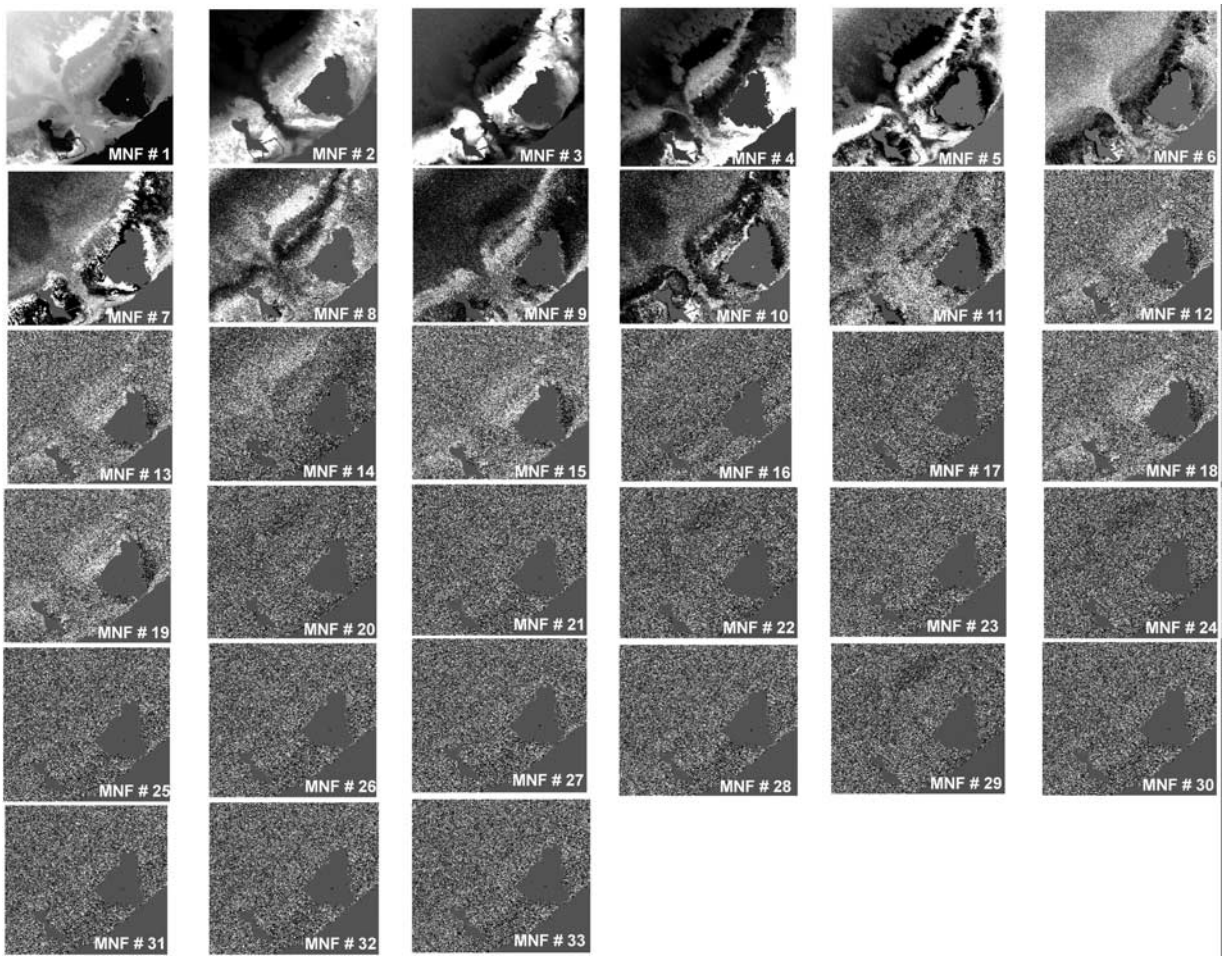

Figure 14. Visual comparison of MNF-transformed bands to identify information bands.

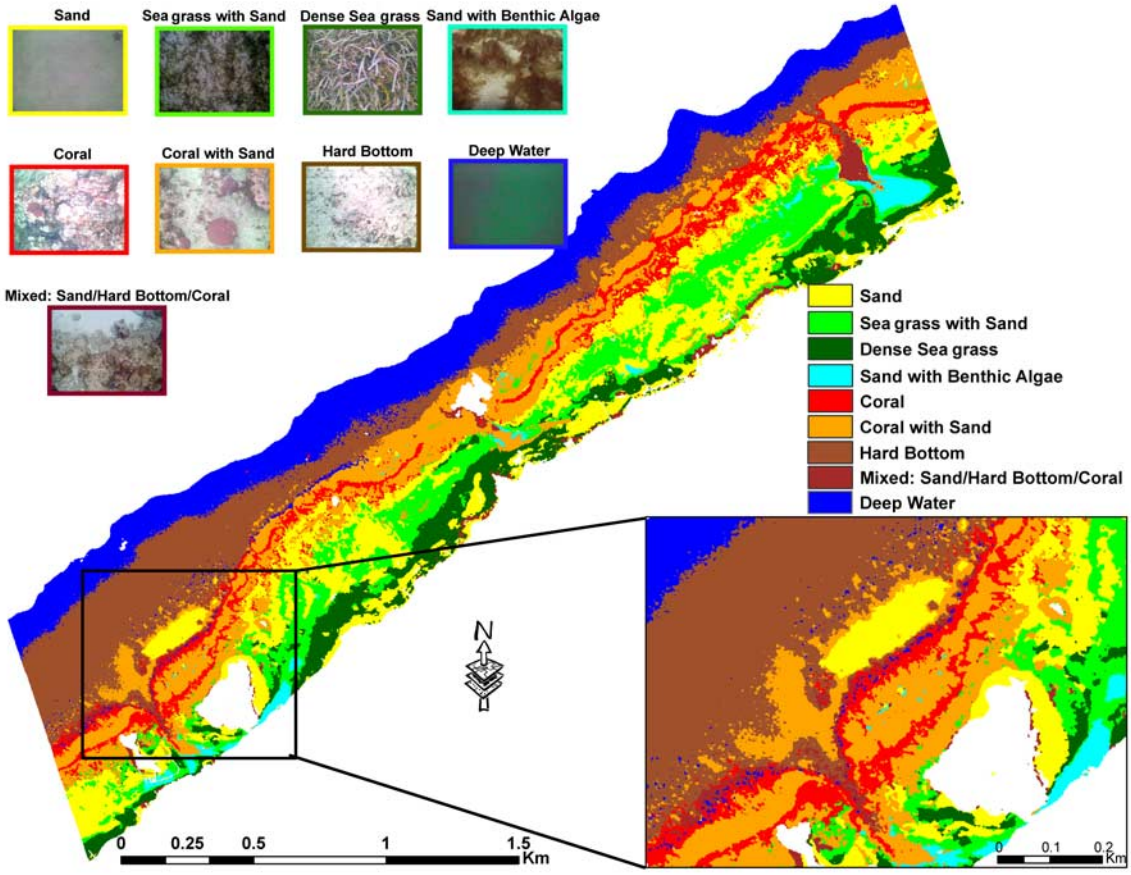

Figure 15. Color-coded map showing different benthic habitats off the coast of Roatan Island, Honduras. This map resulted from an unsupervised classification of the above shown bottom albedo image. The border color of each representative photograph of bottom types (acquired by towfish) matches the color given to a particular class.

the same set of spectra showed spectral features and the magnitude of the ρ was comparable to the in situ spectra.

[33] Since we did not have the required field measurements, the validation for water column correction, that is, for the estimated bottom albedo, was performed in a unique way. For this purpose our hypothesis was, if the water column correction to derive bottom albedo was accurately performed, then the depth factor on the bottom reflectance would have been eliminated and the bottom albedo for a particular bottom types at various depths would be similar. For this purpose, five bottom albedo spectra of coral, sand, and sea grass at different depths were plotted and compared

Table 2. Results of Accuracy Assessment Based on 1208 Underwater Reference Points[a]

Benthic Type	Sand	Sea Grass With Sand	Dense Sea Grass	Sand With Benthic Algae	Coral	Coral With Sand	Hard Bottom	Mixed: Sand/Hard Bottom/Coral	Deep Water	Row Total	Producers' Accuracy, %	Users' Accuracy, %	Kappa Coefficient
Sand	228	5	1	3	5	5	6	1	0	254	87.692	89.764	0.828
Sea grass with sand	5	138	4	4	4	9	3	1	2	170	86.250	81.176	0.833
Dense sea grass	0	4	114	7	4	2	1	0	7	139	87.023	82.014	0.834
Sand with benthic algae	3	3	2	39	2	0	1	2	1	53	65.000	73.585	0.836
Coral	5	2	3	3	187	8	4	3	2	217	85.780	86.175	0.831
Coral with sand	11	5	3	2	11	165	3	5	0	205	85.938	80.488	0.832
Hard bottom	6	2	0	1	3	2	59	3	1	77	75.641	76.623	0.835
Mixed: sand/hard bottom/coral	2	1	0	0	2	1	1	28	0	35	63.636	80.000	0.836
Deep water	0	0	4	1	0	0	0	1	52	58	80.000	89.655	0.836
Column total	260	160	131	60	218	192	78	44	65	Total = 1208			

[a]The classification results showed an overall accuracy of 83.609%, whereas the overall kappa was found to be 0.808.

with their corresponding reflectance spectra before the water column correction (Figure 12). Before the water column correction, water depth played an important role in determining the reflectance values of the bottom, for example, the deeper the bottom the lower the reflectance values. After water column correction, the albedo values for a particular bottom type were close to each other irrespective of their depths. However, it was noted that with increasing depth, dark bottoms or bottoms with high phytoplankton content (corals and sea grass) showed that influence of water column is not completely eliminated. For example, the coral albedo at 5.632 m and 7.421 m and the sea grass albedo at 4.868 m did not reveal the 675 nm chlorophyll absorption feature which was clearly present at other depths (Figure 12). Sand, being the bright bottom, showed a close match for albedos at different depths indicating an accurate water column correction. Another concern with the bottom albedo image was the low signal-to-noise ratio for dark bottoms at longer wavelengths (specifically $\lambda > 600$ nm). This noise was introduced to the image during subsequent calculation and needed to be removed before applying the clustering algorithm to map the benthic habitat.

[34] MNF is a linear transformation related to principal components that orders the data according to signal-to-noise ratio [*Green et al.*, 1988] and can be used to partition the data space into two parts: one associated with large eigenvalues and coherent eigenimages, and a second with near-unity eigenvalues and noise-dominated images. By using only the coherent portions in subsequent processing, the noise is separated from the data, thus improving spectral processing results. The MNF algorithm was used to separate information from noise on the basis of eigenvalues which showed high variability (standard deviation, $\sigma > 46.671$) ranging from 249.005 (component 1) to 1.119 (component 33) (Figure 13). The threshold band separating signal from noise was set on MNF band 10 after examining the σ of eigenvalues and the image. The eigenvalues showed significant variation from band 1 to 10 (range = 249.005–2.318; σ = 79.010) but remained fairly constant (near-unity) from band 11 to 33 (range = 1.558–1.119; σ = 0.103). Visual examination of all the 33 MNF bands also exhibited a clear distinction between bottom albedo signal or coherent eigenimage (MNF bands 1–10) and noise dominated images (MNF bands 11–33) (Figure 14). The first 10 MNF bands were subset from MNF image and were then used in the ISODATA clustering algorithm. An ISODATA classification algorithm was applied to the bottom albedo image resulting 300 clusters and each cluster was assigned to a particular benthic class using in situ data, towfish images, and still photographs derived from the video camera (Figure 15). A comparative evaluation of the classified image versus 1208 independent in situ points (GPS location, towfish image) revealed an overall accuracy of 83.609% (Table 2). An examination of producer's and user's accuracies also showed better classification results with AISA hyperspectral data versus those derived from IKONOS [*Mishra et al.*, 2005], and Landsat TM or SPOT XS data [*Mumby et al.*, 1998b]. Sand, sea grass sand, coral, and deep water areas showed highest producer's and user's accuracies, when compared to sand with benthic algae, hard bottom, and mixed: sand/hard bottom/coral areas. This indicates that confusion between the latter classes during the ISODATA classification were high, because of their similar spectral characteristics. Sand (very bright), sea grass, coral, and deep water (very dark) are the spectrally distinct classes, with the highest spectral separability and lowest classification error. The overall kappa statistic, a discrete multivariate accuracy assessment technique described by *Congalton and Mead* [1983], was 0.808 (Table 2). This statistic estimates the percent of successful classifications compared to a random, chance classification assignment [*Jensen*, 2004]. There are several reasons for the confusion error in the three classes (mentioned above), including spectral overlaps between optically similar objects. For example, the calcium carbonate skeleton of a dead coral (hard bottom) is optically similar to sparse sea grass with a sand background, while algal overgrowth (sand/benthic algae) is often similar to zooxanthalle densities and pigmentation occurring in coral features. The major problem with our classification was primarily associated with the presence of sand in reef areas, and from rapid changes of coral diversity and reef features over relatively short distances, often in areas of patch reefs.

5. Conclusions

[35] This research using AISA Eagle hyperspectral data to map shallow marine benthic habitats, demonstrates the viability of semi-analytical models originally developed by oceanographers and represents a step forward from the previous study carried out by the authors on multispectral satellite sensor (e.g., IKONOS, QuickBird) [*Mishra et al.*, 2005, 2006]. The progression from multispectral to hyperspectral data provided the capability to distinguish between closely related bottom types such as hard bottom, and sand with benthic algae.

[36] One of the most important factors affecting accurate benthic habitat mapping in a coral reef environment is the effect of the water column on the reflectance properties of coral ecosystems. Our research showed that specific spectral features (e.g., pigment absorption) of different bottom types are generally overshadowed by significant water absorption, which makes benthic habitat mapping a difficult task. There is always a temptation among scientists to interpret readily observable variations in remotely sensed color of water as a direct indicator of water quality, or benthic type, without correcting for water column effects. Initially, remote sensing specialists attempted to develop strategies to monitor the extent and vitality of coral reefs, often by assuming the effects of the water column above to be horizontally and vertically homogeneous [*Holden and LeDrew*, 2001]. More recently, investigators have determined these assumptions of homogeneity to be overly simplistic. Our research provides indications that further processing (i.e., water column correction) of airborne or space-borne remotely sensed images is necessary for benthic habitat mapping.

[37] **Acknowledgments.** The authors appreciate the assistance of the Galindo family and the staff of Anthony's Key Resort, Roatan Island, Honduras. We also thank the staff at the Roatan Institute for Marine Science, especially Jennifer Keck, for their assistance and the use of facilities during our field work at that location. The funding for this work was provided by the Center for Advanced Land Management Information Technologies (CALMIT), the University of Nebraska Research Council, and the School of Natural Resources, University of Nebraska-Lincoln.

References

Austin, R. W., and T. J. Petzold (1986), The determination of the diffuse attenuation coefficient of sea water using the Coastal Zone Color Scanner, in *Oceanography From Space*, edited by J. F. R. Gower, pp. 239–256, Plenum, New York.

Bierworth, P. N., T. Lee, and R. Burne (1993), Shallow sea-floor reflectance and water depth derived by unmixing multispectral imagery, *Photogramm. Eng. Remote Sens.*, *59*(3), 331–338.

Biña, R. T., K. Carpenter, W. Zacher, R. Jara, and J. B. Lim (1979), Coral reef mapping using Landsat data: Follow-up studies, *Proc. 12th Int. Symp. Remote Sens. Environ.*, *1*, 2051–2070.

Clark, C., H. Ripley, E. Green, A. Edwards, and P. Mumby (1997), Mapping and measurement of tropical coastal environments with hyperspectral and high spatial resolution data, *Int. J. Remote Sens.*, *18*(2), 237–242.

Clark, C., P. Mumby, J. Chisholm, J. Jaubert, and S. Andrefouet (2000), Spectral discrimination of coral mortality states following a severe bleaching event, *Int. J. Remote Sens.*, *21*(11), 2321–2327.

Congalton, R. G., and R. A. Mead (1983), A quantitative method to test for consistency and correctness in photointerpretation, *Photogramm. Eng. Remote Sens.*, *49*(1), 69–74.

Dove, S. G., M. Takabayashi, and O. Hoegh-Guldberg (1995), Isolation and partial characterization of the pink and blue pigments of Pocilloporid and Acroporid corals, *Biol. Bull.*, *189*, 288–297.

Dustan, P., and J. C. Halas (1987), Changes in the reef-coral community of Carysfort Reef, Key Largo, Florida: 1974 to 1982, *Coral Reefs*, *6*, 91–106.

Gao, B. C., M. J. Montes, Z. Ahmad, and C. O. Davis (2000), Atmospheric correction algorithm for hyperspectral remote sensing of ocean color from space, *Appl. Opt.*, *39*(6), 887–896.

Goodman, J. A., M. Montes, and S. Ustin (2003), Applying TAFKAA for atmospheric correction of AVIRIS over coral ecosystems in the Hawaiian islands, paper presented at 12th Airborne Geoscience Workshop, Jet Propul. Lab., Pasadena, Calif., 24 –28 Feb.

Gordon, H. R., and O. B. Brown (1974), Influence of bottom albedo on the diffuse reflectance of a flat homogeneous ocean, *Appl. Opt.*, *13*, 2153–2159.

Gordon, H. R., and A. Y. Morel (1983), *Remote Assessment of Ocean Color for Interpretation of Satellite Visible Imagery: A Review of Lecture Notes on Coastal and Estuarine Studies*, 113 pp., Springer-Verlag, New York.

Gordon, H. R., O. B. Brown, R. H. Evans, J. W. Brown, R. C. Smith, K. S. Baker, and D. K. Clark (1988), A semianalytic radiance model of ocean color, *J. Geophys. Res.*, *93*(D9), 10,909–10,924.

Green, A. A., M. Berman, B. Switzer, and M. D. Craig (1988), A transformation for ordering multispectral data in terms of image quality with implications for noise removal, *IEEE Trans. Geosci. Remote Sens.*, *26*(1), 65–74.

Hochberg, E. J., and M. J. Atkinson (2000), Spectral discrimination of coral reef benthic communities, *Coral Reefs*, *19*, 164–171.

Holasek, R. F., E. D. Portigal, P. Johnson, M. Segava, G. Susner, and C. Hill (1998), Coral and substrate mapping in Kaneohe Bay, Oahu, Hawaii using the advanced airborne hyperspectral imaging system (AAHIS), *Proc. 5th Int. Conf. Remote Sens. Mar. Coastal Environ.*, *1*, 177–186.

Holden, H., and E. LeDrew (1998), The scientific issues surrounding remote detection of submerged coral ecosystems, *Prog. Phys. Geogr.*, *22*(2), 190–221.

Holden, H., and E. LeDrew (1999), Hyperspectral identification of coral reef features, *Int. J. Remote Sens.*, *20*(13), 2545–2563.

Holden, H., and E. LeDrew (2000), Accuracy assessment of hyperspectral classification of coral reef features based on first and second derivatives, *Geocarto Int.*, *15*(2), 5–11.

Holden, H., and E. LeDrew (2001), Effects of the water column on hyperspectral reflectance of submerged coral reef features, *Bull. Mar. Sci.*, *69*(2), 685–699.

Holden, H., and E. LeDrew (2002), Measuring and modeling water column effects on hyperspectral reflectance in a coral reef environment, *Remote Sens. Environ.*, *81*, 300–308.

Jensen, J. R. (2004), *Introductory Digital Image Processing: A Remote Sensing Perspective*, 526 pp., Prentice-Hall, Upper Saddle River, N. J.

Jensen, J. R., S. Narumalani, O. Weatherbee, and H. E. Mackey (1991), Remote sensing offers an alternative for mapping wetlands, *Geo Inf. Syst.*, *1*, 46–53.

Jupp, D. L. B. (1986), The application and potential of remote sensing in the Great Barrier Reef region, research publication, 56 pp., Great Barrier Reef Mar. Park Auth., Townsville, Qld., Australia.

Jupp, D. L. B., K. Mayo, D. Kuchler, S. Heggen, W. Kendall, B. Radke, and T. Ayling (1985), Remote sensing for planning and managing the Great Barrier Reef of Australia, *Photogrammetria*, *40*, 21–42.

Keck, J. (2000), Instructor's guide, 70 pp., Roatan Inst. for Mar. Sci., Roatan, Bay Islands, Honduras.

Kuchler, D. A., R. T. Biña, and D. R. van Claasen (1988), Status of high-technology remote sensing for mapping and monitoring coral reef environments, *Proc. 6th Int. Coral Reef Symp.*, *1*, 97–101.

Kutser, T., A. G. Dekker, and W. Skirving (2003), Modeling spectral discrimination of Great Barrier Reef benthic communities by remote sensing instruments, *Limnol. Oceanogr.*, *48*(1), 497–510.

Lee, Z., K. L. Carder, S. K. Hawes, R. G. Steward, T. G. Peacock, and C. O. Davis (1994), A model for interpretation of hyperspectral remote-sensing reflectance, *Appl. Opt.*, *33*, 5721–5732.

Lee, Z., K. L. Carder, R. G. Steward, T. G. Peacock, C. O. Davis, and J. L. Mueller (1996), Remote-sensing reflectance and inherent optical properties of oceanic waters derived from above-water measurements, *Proc. SPIE*, *2963*, 160–166.

Lee, Z. P., K. L. Carder, C. D. Mobley, R. G. Steward, and J. S. Patch (1998), Hyperspectral remote sensing for shallow waters. 1. A semianalytical model, *Appl. Opt.*, *37*, 6228–6329.

Lyzenga, D. (1978), Passive remote sensing techniques for mapping water depth and bottom features, *Appl. Opt.*, *17*, 379–383.

Lyzenga, D. (1981), Remote sensing of bottom reflectance and water attenuation parameters in shallow water sign aircraft and Landsat data, *Int. J. Remote Sens.*, *2*, 71–82.

Mäkisara, K., A. Lohi, and J. P. Kärnä (1994), A system for geometric and radiometric correction of airborne imaging spectrometer data, in *1994 International Geoscience Remote Sensing Symposium*, pp. 851–853, Geosci. and Remote Sens. Soc., Piscataway, N. J.

Maritorena, S., A. Morel, and B. Gentili (1994), Diffuse reflectance of oceanic shallow waters: Influence of water depth and bottom albedo, *Limnol. Oceanogr.*, *39*, 1689–1703.

Matthew, M. W., S. M. Adler-Golden, A. Berk, G. Felde, G. P. Anderson, D. Gorodestzky, S. Paswaters, and M. Shippert (2003), Atmospheric correction of spectral imagery: Evaluation of the FLAASH algorithm with AVIRIS data, *Proc. SPIE*, *IX*(5093), 474–482.

Mishra, D. R., S. Narumalani, D. Rundquist, and M. Lawson (2005), High resolution ocean color remote sensing of benthic habitats: A case study at the Roatan Island, Honduras, *IEEE Trans. Geosci. Remote Sens.*, *43*(7), 1592–1604.

Mishra, D. R., S. Narumalani, D. Rundquist, and M. P. Lawson (2006), Benthic habitat mapping in tropical marine environments using QuickBird imagery, *Photogramm. Eng. Remote Sens.*, *72*(9), 1037–1048.

Mobley, C. D. (1994), *Light and Water: Radiative Transfer in Natural Waters*, 592 pp., Academic, San Diego, Calif.

Mobley, C. D., B. Gentili, H. R. Gordon, Z. Jin, G. W. Katawar, A. Morel, P. Reinersman, K. Stamnes, and R. H. Stavn (1993), Comparison of numerical models for computing underwater light fields, *Appl. Opt.*, *36*, 7484–7504.

Mobley, C. D., H. Zhang, and K. J. Voss (2003), Effects of optically shallow bottoms on upwelling radiances: Bidirectional reflectance distribution function effects, *Limnol. Oceanogr.*, *48*(1), 335–337.

Morel, A. (1974), Optical properties of pure water and pure seawater, in *Optical Aspects of Oceanography*, edited by N. G. Jerlov and E. Steeman Nielsen, pp. 1–24, Academic, San Diego, Calif.

Morel, A. (1988), Optical modeling of the upper ocean in relation to its biogenous matter content (case 1 waters), *J. Geophys. Res.*, *93*, 10,749–10,768.

Morel, A. Y., and B. Gentili (1993), Diffuse reflectance of oceanic waters, II. Bi-directional aspects, *Appl. Opt.*, *32*(33), 6864–6879.

Mumby, P. J., E. P. Green, C. D. Clark, and A. J. Edwards (1998a), Digital analysis of multispectral airborne imagery of coral reefs, *Coral Reefs*, *17*, 59–69.

Mumby, P. J., C. Clark, E. Green, and A. Edwards (1998b), Benefits of water column correction and contextual editing for mapping coral reefs, *Int. J. Remote Sens.*, *19*(1), 203–210.

Myers, M., J. Hardy, C. Mazel, and P. Dustan (1999), Optical spectra and pigmentation of Caribbean reef corals and macroalgae, *Coral Reefs*, *18*(2), 179–186.

Philpot, W. D. (1989), Bathymetric mapping with passive multispectral imagery, *Appl. Opt.*, *28*, 1569–1578.

Pope, R. M., and E. S. Fry (1997), Absorption spectrum (380–700 Nm) of pure water. 2. Integrating cavity measurements, *Appl. Opt.*, *36*, 8710–8723.

Stumpf, R. P., K. Holderied, and M. Sinclair (2003), Determination of water depth with high-resolution satellite imagery over variable bottom types, *Limnol. Oceanogr.*, *48*, 547–556.

Vermote, E. F., D. Tanre, J. L. Deuze, M. Herman, and J. J. Morcrette (1994), *Second Simulation of the Satellite Signal in the Solar Spectrum (6S)*, version 6.0, 134 pp., NASA Goddard Space Flight Cent., Greenbelt, Md.

Young, L. R., K. L. Carder, R. G. Stewart, and F. R. Chen (1995), Comparison of measured and modeled bottom reflectance spectra on the southeastern shelf of the Florida Keys, *Proc. SPIE*, *2480*, 237–247.

Zhang, M., K. L. Carder, F. E. Muller-Karger, Z. Lee, and D. B. Goldgof (1999), Noise reduction and atmospheric correction for coastal applications of Landsat thematic mapper imagery, *Remote Sens. Environ.*, *70*, 167–180.

M. Lawson and R. Perk, Department of Geosciences, 306 Bessey Hall, University of Nebraska, Lincoln, NE 68588-0340, USA.

D. R. Mishra, S. Narumalani, and D. Rundquist, Center for Advanced Land Management Information Technologies, School of Natural Resources, Hardin Hall, University of Nebraska, Lincoln, NE 68583-0973, USA. (dmishra@calmit.unl.edu)